

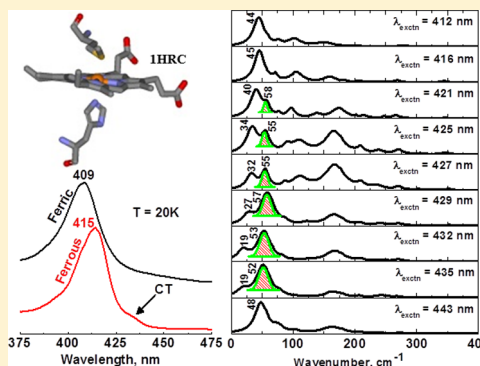
# Investigations of the Low Frequency Modes of Ferric Cytochrome *c* Using Vibrational Coherence Spectroscopy

Venugopal Karunakaran,<sup>†,‡</sup> Yuhan Sun,<sup>†</sup> Abdelkrim Benabbas, and Paul M. Champion\*

Department of Physics and Center for Interdisciplinary Research on Complex Systems, Northeastern University, Boston, Massachusetts 02115, United States

## Supporting Information

**ABSTRACT:** Femtosecond vibrational coherence spectroscopy is used to investigate the low frequency vibrational dynamics of the electron transfer heme protein, cytochrome *c* (cyt *c*). The vibrational coherence spectra of ferric cyt *c* have been measured as a function of excitation wavelength within the Soret band. Vibrational coherence spectra obtained with excitation between 412 and 421 nm display a strong mode at  $\sim 44\text{ cm}^{-1}$  that has been assigned to have a significant contribution from heme ruffling motion in the electronic ground state. This assignment is based partially on the presence of a large heme ruffling distortion in the normal coordinate structural decomposition (NSD) analysis of the X-ray crystal structures. When the excitation wavelength is moved into the  $\sim 421\text{--}435\text{ nm}$  region, the transient absorption increases along with the relative intensity of two modes near  $\sim 55$  and  $30\text{ cm}^{-1}$ . The intensity of the mode near  $44\text{ cm}^{-1}$  appears to minimize in this region and then recover (but with an opposite phase compared to the blue excitation) when the laser is tuned to 443 nm. These observations are consistent with the superposition of both ground and excited state coherence in the  $421\text{--}435\text{ nm}$  region due to the excitation of a weak porphyrin-to-iron charge transfer (CT) state, which has a lifetime long enough to observe vibrational coherence. The mode near  $55\text{ cm}^{-1}$  is suggested to arise from ruffling in a transient CT state that has a less ruffled heme due to its iron  $d^6$  configuration.



## INTRODUCTION

Cytochrome *c* (cyt *c*) is a water-soluble globular and membrane-associated heme protein located in the intermembrane space of the mitochondria. It serves its redox function by transferring an electron from the  $bc_1$  complex to the terminal electron acceptor, cytochrome *c* oxidase. It is also involved in both pre- and postapoptosis processes.<sup>1</sup> The X-ray structure of ferric horse heart (hh) cyt *c* (PDB ID 1HRC) is shown in Figure 1. The protein is composed of 104 amino acids and contains the heme as a prosthetic group, which is covalently attached to the polypeptide chain through two thioether bonds with residues Cys14 and Cys17. The heme iron in cyt *c* is low-spin and 6-coordinate with axial ligands His18 and Met80. Extensive research has been carried out on cyt *c* over the last four decades<sup>2,3</sup> using different spectroscopic techniques that include optical pump–probe spectroscopy,<sup>4–9</sup> nuclear magnetic resonance spectroscopy,<sup>10</sup> electron paramagnetic resonance spectroscopy,<sup>11</sup> Mössbauer spectroscopy,<sup>11,12</sup> steady state<sup>13</sup> and time-resolved Raman spectroscopy,<sup>14</sup> nuclear resonance vibrational spectroscopy,<sup>15,16</sup> inelastic X-ray scattering,<sup>17</sup> vibrational coherence spectroscopy,<sup>6</sup> and fluorescence up-conversion.<sup>8,9,18</sup>

In earlier studies of ferrous cyt *c*, using femtosecond transient absorption spectroscopy, Wang et al.<sup>6</sup> observed the photolysis of the axial Met80 ligand and measured the rebinding time constant to be 6.2 ps. This assignment was based on the close resemblance of transient absorption spectra of ferrous cyt *c* to

that of a model 5-coordinate (5c) histidine ligated complex, ferrous microperoxidase (MP-8), and on the appearance of the Fe–His stretching vibration at  $\sim 220\text{ cm}^{-1}$  in the vibrational coherence spectrum of the ferrous cyt *c*. Negrier et al. studied the ultrafast dynamics of heme in both ferric and ferrous cyt *c* using femtosecond transient absorption and sub-picosecond time-resolved resonance Raman spectroscopy.<sup>4,14</sup> They confirmed the photodissociation of Met80 in ferrous cyt *c* and observed its rebinding to the 5c high-spin (HS) photoproduct with a time constant of 4.8 ps. The photodissociation of Met80 was further evidenced by the appearance of the  $\nu_{\text{Fe–His}}$  mode at  $216\text{ cm}^{-1}$  and the down-shifts of the high-frequency ( $1300\text{--}1700\text{ cm}^{-1}$ ) marker bands in the transient Raman spectra.<sup>4</sup>

In contrast, the ferric form of cyt *c* does not appear to undergo photodissociation, and the optical transients are dominated by intramolecular vibrational energy redistribution ( $<1\text{ ps}$ ) with subsequent intermolecular vibrational energy transfer ( $\sim 4\text{ ps}$ ) taking place in the ground electronic state vibrational manifold of the heme.<sup>4</sup> Lowenich et al.<sup>7</sup> reinvestigated the photoreduction of ferric cyt *c* using femtosecond and nanosecond transient absorption spectroscopy and postulated a relaxation pathway leading to a hot ground

Received: February 5, 2014

Revised: May 12, 2014

Published: May 13, 2014

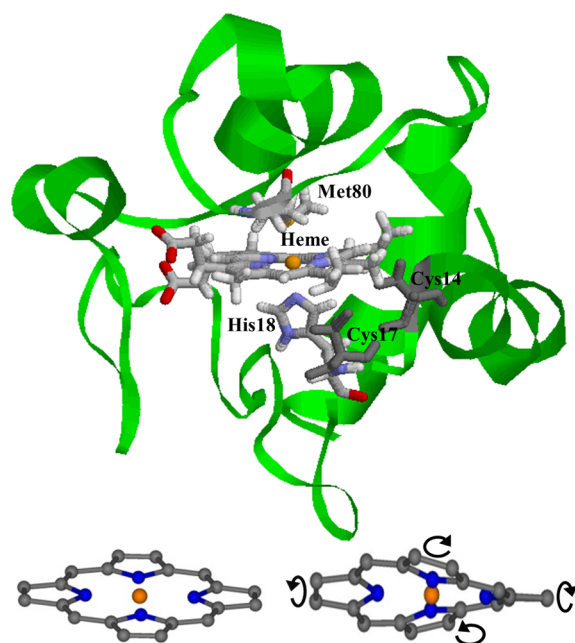


**Figure 1.** Crystal structures of horse heart ferric cyt *c* generated from PDB 1HRC. The heme prosthetic group, its axial ligands His18 and Met80, and the two cysteine residues (Cys14 and Cys17) that form thioether bridges to the heme are shown in the stick model. The planar Fe-porphine core and its ruffling distortion are also shown. Ruffling involves motions with alternating clockwise and counter-clockwise twisting of the pyrrole rings along the Fe–N axes.

state following  $\sim 0.3$  ps of internal conversion. The hot ground state of the chromophore was suggested to cool with a time constant of  $\sim 4$  ps and the formation of a ferrous population was observed on the same time scale, indicating the system might be undergoing some sort of thermally enhanced electron transport process.<sup>7</sup> However, this model appears to invoke a transiently hot acceptor, rather than a hot donor state, which will have uncertain effects on the donor-to-acceptor transport rate.

Zang et al.<sup>5</sup> differentiated the heme dynamics and the induced protein conformational relaxations between ferric and ferrous cyt *c* by using femtosecond pump–probe spectroscopy. In the ferrous cyt *c*, the photodissociation of the distal Met80 ligand creates a strong global protein “quake” that recovers in 42 ps, following a 13 ps heme relaxation. The global conformational relaxation was not observed in the ferric state of cyt *c*.<sup>5</sup> More recently, Chergui et al.<sup>8</sup> investigated the energy transfer and electronic relaxation of ferrous and ferric cyt *c* using broadband UV–vis femtosecond transient absorption spectroscopy and a fluorescence up-conversion technique with excitation at various wavelengths in the visible (400 and 530 nm) and the UV (286 nm) region. It was proposed that charge transfer from the excited states of the porphyrin ring to the  $d_z^2$  antibonding orbital of the iron induce photolysis in the ferrous form. In contrast, the partially unoccupied  $d_\pi$  orbital in the ferric form offers an alternative, and faster, decay channel which prevents the Met80 photolysis.<sup>8,9</sup>

It is known that the heme cofactor in the cyt *c*-type proteins is strongly distorted along the ruffling coordinate, and the out-of-plane (OOP) distortions have been systematically determined on the basis of normal coordinate structural decomposition (NSD) of the porphyrin.<sup>19</sup> The cause of heme distortion arises from the forces imposed by the protein

backbone through steric crowding and from the covalent linkages and H-bonding between the protein residues (in the CXXCH motif) and the heme.<sup>20,21</sup> The OOP distortions are conserved in heme proteins and have been correlated to the protein function.<sup>22</sup> For example, the ruffling distortion is thought to be involved in controlling the redox potentials,<sup>23–25</sup> based upon its appearance in the electron transfer<sup>24,26,27</sup> (e.g., cytochrome *c*) and NO sensor<sup>28</sup> (e.g., nitrophorins) proteins. Saddling distortions have been suggested to be involved in spin state changes,<sup>29–31</sup> and they are commonly found in peroxidases and oxidases (e.g., horseradish peroxidase and cytochrome P450<sub>cam</sub>). It is also noteworthy that a functionally important “doming” distortion, due to the iron atom displacement from the heme plane, appears in the oxygen storage or transport proteins (e.g., myoglobin, hemoglobin).<sup>32,33</sup>

Recently, Liptak et al. modified the degree of ruffling in the heme of *Hydrogenobacter thermophilus* (Ht) cytochrome  $c_{552}$  by mutation and demonstrated a correlation between the heme ruffling and the  $^{13}\text{C}$  and  $^1\text{H}$  nuclear magnetic resonance (NMR) hyperfine shifts of the heme.<sup>10</sup> Because the heme ruffling deformation disrupts the  $d\pi$  and porphyrin  $\pi$  overlap, it localizes both the unpaired iron electron and its “hole-state” on the ferric iron atom. When the hole is on the heme periphery, it can significantly increase the overlap with the donor state electron, whereas, when it is localized on the iron atom, the tunnel distance is longer, which slows the rate of electron transfer from its redox partner.<sup>34</sup> The ruffling distortion can also lower the reduction potential of the heme by altering the energy levels of the  $d$  orbitals.<sup>10,35</sup> This is consistent with the observation that the reduction potential of highly ruffled *Pa* cyt  $c_{551}$  F7A is 100 mV lower than the less ruffled wild type.<sup>10</sup> This relationship is also in good agreement with the investigation by Marletta et al.<sup>36</sup> on the heme nitric oxide/oxygen binding protein from the thermophilic bacterium *Thermoanaerobacter tengcongensis* and with early measurements on nitrophorin,<sup>28</sup> which is unusual in that it remains in the ferric state upon NO binding.

A variety of investigations<sup>21,28,33,34,37–39</sup> involving the low-frequency vibrational dynamics of heme proteins have demonstrated that impulsive stimulated Raman<sup>40</sup> driven vibrational coherence, or vibrational coherence spectroscopy (VCS), is a sensitive probe of the thermally accessible and functionally relevant distortions of the active site heme chromophore. In the following, we use vibrational coherence spectroscopy to probe the low frequency vibrational dynamics of ferric cyt *c* in the region below  $400\text{ cm}^{-1}$ . The observed low frequency modes compare favorably to the steady state resonance Raman spectra in the energy range that is mutually accessible ( $200\text{--}400\text{ cm}^{-1}$ ). An investigation of changes in the low-frequency vibrational coherence activity as a function of excitation wavelength suggests the presence of a charge transfer state with an upshifted ruffling frequency arising from the transient population of a  $d^6$  iron atom.

## ■ EXPERIMENTAL SECTION

**Sample Preparation.** Horse heart (hh) cyt *c* was purchased from Sigma-Aldrich and used without further purification. The ferrous cyt *c* used in control experiments was prepared by reducing ferric cyt *c* in 0.1 M KPi buffer at pH 7.0 using a small amount of saturated sodium dithionite solution under anaerobic conditions. For vibrational coherence spectroscopy, the concentration of the protein samples was

adjusted so that the optical density of the sample at the pump wavelength was between 0.7 and 1.0 O.D. in a 1 mm optical path-length spinning sample cell. Given the large range of the excitation wavelengths employed for excitation profile measurements (from 412 to 443 nm), the final concentration was between 50 and 200  $\mu\text{M}$ . The absorption spectra of all samples were recorded before and after the experiments to check the integrity of the sample and no differences were observed.

**Optical System.** The details of VCS have been discussed elsewhere,<sup>28,32,33,41–43</sup> along with the experimental optical system,<sup>33,38,42,44</sup> and further details are given in the Supporting Information. Two different detection geometries, each providing for optimal enhancement of a different range of frequencies, are used to obtain the vibrational coherence spectra. In the open-band detection scheme, a Si photodiode is used to measure the entire spectral bandwidth of the probe pulse which optimizes the fidelity of the low frequency response in the range 20–100  $\text{cm}^{-1}$ . The detuned detection scheme selectively enhances the higher frequency response in the coherent signal<sup>33,38,42,45</sup> with improved reliability in the  $\sim 200$ –400  $\text{cm}^{-1}$  region. The detuned detection configuration is accomplished using a monochromator that typically detects a bandwidth of 0.5 nm that is  $\sim 5$  nm away from the carrier frequency (central wavelength) of the probe pulse. The results obtained from the detuned configuration allow direct comparison to frequency domain techniques like resonance Raman spectroscopy, which probe modes above  $\sim 200$   $\text{cm}^{-1}$ .

**Data Analysis.** The experimental data have components arising from population transfer as well as vibrational coherence. The residual coherence signal is obtained by removing the nonrecursive population decay components. Digitization of the experimental signal is done using a lock-in amplifier (LIA) on a 24-bit scale, allowing for a sufficient dynamic range to resolve the low amplitude coherence signals. The fractional change of transmittance,  $\Delta T/T$ , for the open band oscillatory signals is on the order of  $10^{-4}$ – $10^{-5}$ . We used linear predictive singular value decomposition (LPSVD) to analyze the data, which simultaneously fits the exponential decays associated with the population dynamics and the damped cosine functions that describe the vibrational oscillations.

**Resonance Raman Spectra.** Resonance Raman spectra were obtained using a standard setup with a  $90^\circ$  light-collection geometry and a single grating monochromator (Acton SP2500 with 1800 g/mm holographic UV optimized grating; Princeton Instruments, Princeton, NJ). An optical polarization scrambler was inserted in front of the monochromator to obtain the intensity of the scattered light without bias from the polarization-sensitive grating. The monochromator output was coupled to a liquid-nitrogen-cooled CCD (SPEX 10:400B, Princeton Instruments, Princeton, NJ). In order to improve detection in the low-frequency domain of Raman shifts, an interferometric notch filter (Kaiser Optical Systems, Ann Arbor, MI) was used to extinguish the elastically and quasi-elastically scattered laser light. Samples were excited with a 413.1 nm laser line generated by a krypton laser (Innova 300, Coherent) with a power of  $\sim 6$  mW. A standard quartz cuvette (NSG Precision Cells, Farmingdale, NY) was used for the experimental Raman measurements. All Raman spectra are frequency calibrated using fenchone with  $\pm 1$   $\text{cm}^{-1}$  spectral resolution.

## RESULTS

The equilibrium absorption spectra of ferric and ferrous cyt *c* are shown in Figure 2. The ferric and ferrous forms show Soret

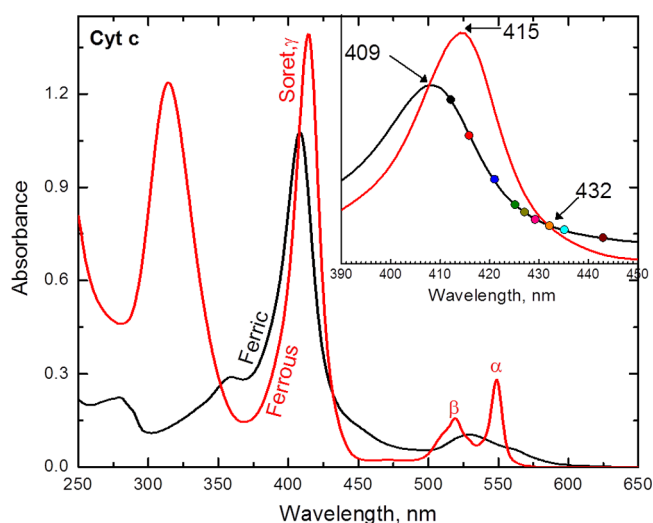


**Figure 2.** Absorption spectra of horse heart ferric (black) and ferrous (red) cyt *c* in 0.1 M potassium phosphate buffer at pH 7.0. The different colored circles in the inset show the different excitation wavelengths used in the VCS study.

absorption maxima at 409 and 415 nm, respectively. The ferric form has a broad asymmetric Q-band near 530 nm, whereas the ferrous form displays a clear splitting of the Q-band into the 0–0 transition ( $\alpha$ -band at 549 nm) and the vibronic 0–1 transitions ( $\beta$ -band at 519 nm). The VCS spectra and the time-resolved transmittance of ferric cyt *c* were obtained at various excitation wavelengths shown by the different colored circles in the inset of Figure 2.

The time-resolved transmission changes following an optical pump pulse are illustrated in Figure 3 for pump–probe excitations from 412 to 443 nm. Here it is important to note that the absolute amplitudes of the vibrational modes from VCS experiments are difficult to independently calibrate in going from one wavelength to another. This is due to a variety of experimental changes that can take place when the laser wavelength is tuned. As a result, we normalized the VCS data using the continuum measurements reported by Negrerie et al.<sup>4</sup> The change in optical transmission at a selected time (600 fs) following the pump pulse is measured in both the VCS and continuum experiments.<sup>4</sup> This allows a wavelength-dependent normalization factor to be extracted from the continuum experiments and used to scale the VCS measurements performed at the different laser wavelengths. Details of this procedure are given in the Supporting Information (Table S2). The vibrational coherences that are excited and coupled to the resonant electronic transition are damped within about 3 ps, due to inhomogeneity, pure dephasing, and vibrational lifetimes. Hence, the kinetic traces are displayed to only 4 ps. The dominant coherence coupling signal near time zero arises from the interaction of the medium and the electric fields of the pump and probe pulses.

The transmission change at 412 nm is consistent with a simple bleaching–recovery signal, whereas, to the red of 416 nm, a transient absorption signal appears on the  $\sim 1$  ps time scale, reaching a maximum near 427 nm. The trend and sign of



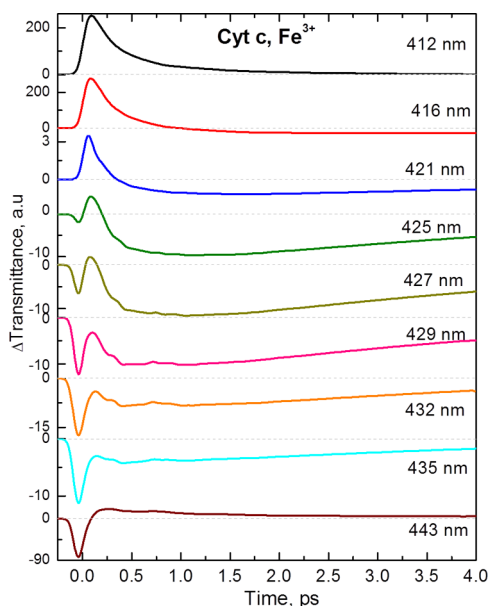


**Figure 3.** Femtosecond time-resolved optical transmittance ( $\Delta T$ ) of ferric cyt *c* at different pump/probe excitation wavelengths. The data at different wavelengths are scaled to match the transient absorption spectrum obtained using a continuum probe<sup>4</sup> at 600 fs. The absolute intensity is in arbitrary units, but the transmittance at each wavelength is self-consistently scaled to the full transient absorption spectrum as given by the vertical axis of each trace.

the pump–probe traces displayed in Figure 3 agree very well with continuum measurements<sup>4</sup> probed at corresponding wavelengths, including the return of the bleach signal at 443 nm. The rate constants and corresponding amplitudes for the nonoscillatory components of the signals (obtained using LPSVD analysis) are given in the Supporting Information (Table S1). The kinetic response for  $t > 0.2$  ps is also consistent with previously reported transient absorption spectra.<sup>4</sup> Because longer time constants are not so reliable in an experiment with a 4 ps time window, the population kinetics at 425 nm were also measured with an 18 ps time window, as shown in the Supporting Information (Figure S2). The major component of the transient absorption signal has a time constant of 4.3 ps, which is consistent with the relaxation time found previously for ferric cyt *c*.<sup>4</sup>

In order to obtain the higher frequency components of the induced third order polarization, we use a “detuned” detection scheme as outlined in the Experimental Section. Figure 4 shows a qualitative correlation between the Raman and coherence spectra for ferric cyt *c*. The measured Raman spectrum (red) is presented at the top of the figure. The Raman spectrum at 413 nm is compared with both open band (green) and detuned (blue) VCS spectra, collected using pulses centered at 432 nm. The detuned measurements integrate the probe pulse over a 0.5 nm spectral bandwidth, which is centered at 427 nm, 5 nm to the blue of the carrier frequency ( $\lambda_{\text{pr}} = 432$  nm). The conventional spontaneous resonance Raman spectra are unable to probe effectively below  $\sim 150$   $\text{cm}^{-1}$  due to limitations brought on by Rayleigh and quasi-elastic light scattering. The inset in Figure 4 shows the oscillatory components of the response (open circles) and the LPSVD fits. As can be seen from the figure, there is a very good correlation between the detuned coherence spectrum and the Raman spectrum in the region from 175 to 400  $\text{cm}^{-1}$ . The modes obtained from the

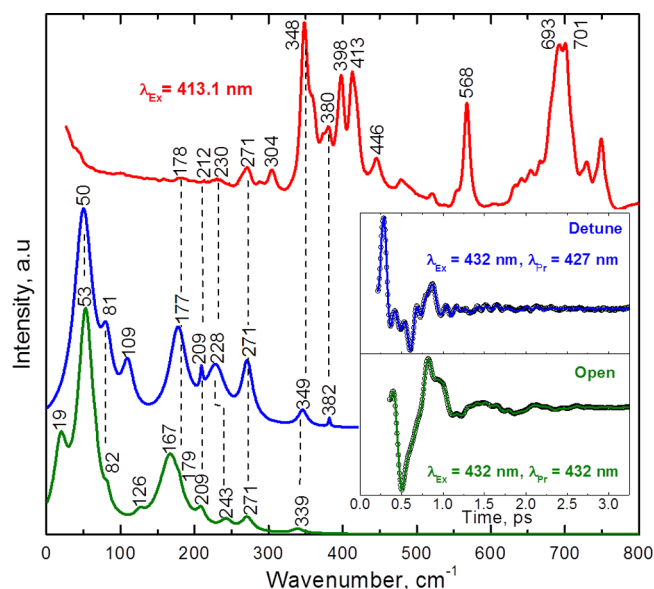


**Figure 4.** Correlation between the Raman and coherence spectra for ferric cyt *c* at pH 7.0. The Raman spectrum (red) was measured with excitation at 413.1 nm, whereas open band (green) and detuned (blue) coherence spectra were measured at a carrier wavelength of 432 nm. The detuned coherence data were collected with a 0.5 nm spectral window, detuned 5 nm to the blue of the carrier wavelength. The time domain oscillatory data are shown in the inset as small circles, and the LPSVD fits are the solid lines through the data. There is a very good correlation between the Raman and coherence spectral frequencies, with an estimated error of roughly  $\pm 3$   $\text{cm}^{-1}$ . The peaks at 271, 304, 348, 380, 398, 413, 446, 568, 693, and 701  $\text{cm}^{-1}$  in the Raman spectra are assigned to  $\nu_9$ ,  $\nu_{51}$ ,  $\nu_8$ ,  $\delta(\text{C}_\beta\text{C}_\alpha\text{C}_\alpha)$ ,  $\delta(\text{C}_\beta\text{C}_\alpha\text{S})$ ,  $\delta(\text{C}_\beta\text{C}_\alpha\text{C}_\beta)$ ,  $\gamma_{22}$ ,  $\gamma_{21}$ ,  $\nu(\text{C}_\alpha\text{S})$ , and  $\nu_7$ , respectively.<sup>13</sup>

Raman spectrum at 178, 212, 230 ( $\gamma_{24}$ ), 271 ( $\nu_9$ ), 348 ( $\nu_8$ ), and 380  $\text{cm}^{-1}$  ( $\delta(\text{C}_\beta\text{C}_\alpha\text{C}_\alpha)$ ) are correlated with the modes at 177, 209, 228, 271, 349, and 382  $\text{cm}^{-1}$  that appear in the detuned coherence spectra (with an accuracy of  $\pm 3$   $\text{cm}^{-1}$ ). The  $\nu_9$  mode appears exactly at 271  $\text{cm}^{-1}$  in all three spectra. We also find a very good correlation between the low frequency modes at 53, 82, 179, and 209  $\text{cm}^{-1}$  when the open-band and detuned detection spectra are compared. Generally, the vibrational modes seen in the VCS spectra at 432 nm appear to be reasonably well-correlated and in agreement with the Raman spectrum at 413 nm. The exception is the mode at 109  $\text{cm}^{-1}$  in the detuned spectrum, which is not observed under open band conditions at 432 nm. However, a mode at 105–110  $\text{cm}^{-1}$  does appear in the open band spectra taken in the 412–427 nm region.

Figure 5 shows the open-band VCS spectra of ferric cyt *c* obtained with excitation at the different wavelengths, which are labeled as colored dots in the absorption spectra shown in Figure 2. The experimental oscillatory signals are normalized so the VCS measurements at differing wavelengths can be more directly compared. This is done using the continuum transmittance,<sup>4</sup> and the normalized intensity information is given by the scale factors on the left panels of each trace in Figure 5 (see also the Supporting Information, Table S2). The right panels show the corresponding spectral components extracted using the LPSVD analysis, and the scale factors on the vertical axis are again obtained by the continuum normalization procedure. The spectra show a strong mode we denote as  $\gamma_a$  ( $\sim 44$   $\text{cm}^{-1}$ ) with excitation at 412 and 416 nm. However, as

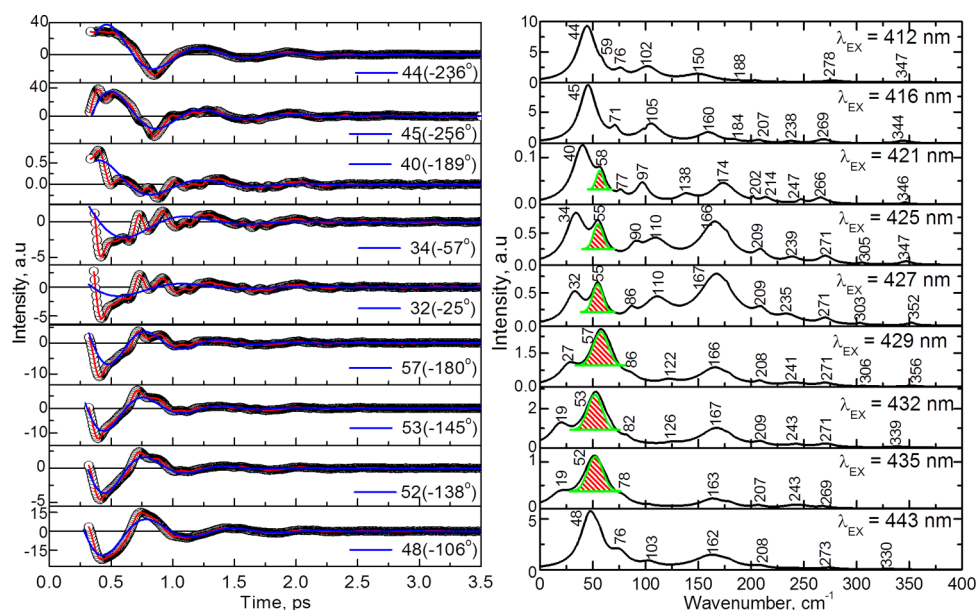


**Figure 5.** Open-band coherence spectra of ferric cyt *c* at different excitation wavelengths. The left panels show the oscillatory components (open circles) and the LPSVD fits (solid red lines). The LPSVD component corresponding to the dominant low-frequency mode and its phase is also shown (blue solid line). The right panels show the corresponding amplitudes of the power spectra. The intensities of the mode near  $\sim 55\text{ cm}^{-1}$  are indicated by the diagonal red lines. The relative scaling factors at each wavelength are obtained by normalizing to the continuum data<sup>4</sup> and are given on the left vertical axis of each panel.

the excitation wavelength is tuned further to the red, between 425 and 435 nm, the  $\gamma_a$  mode is reduced in intensity and a mode near  $\sim 55\text{ cm}^{-1}$  can now be observed (see the Supporting Information, Figure S3), along with a lower frequency mode near  $\sim 30\text{ cm}^{-1}$ .

We label the mode at  $\sim 55\text{ cm}^{-1}$   $\gamma_{a1}$  because of its potential relationship to  $\gamma_a$  at  $\sim 44\text{ cm}^{-1}$  (vide infra). The  $\gamma_{a1}$  mode attains a maximum relative amplitude in the region between 429 and 430 nm, as can be seen in the plot of its absolute intensity as a function of the pump–probe wavelength (see the Supporting Information, Figure S3). When the excitation wavelength is shifted to 443 nm, still further to the red of the Soret absorption band maximum, the strong mode at  $\sim 55\text{ cm}^{-1}$  is again subsumed by the  $\gamma_a$  mode at  $\sim 48\text{ cm}^{-1}$ , which now has a phase that is shifted by roughly  $\pi$  compared to excitation at 412–416 nm (as can be seen from inspection of the coherence signals in the top and bottom panels of Figure 5). The  $\sim 55\text{ cm}^{-1}$  mode is highlighted in Figure 5 by the red cross-hatch depicting the area under the peak (however, the actual intensity of this mode is given by the LPSVD analysis, so no deconvolution of the areas depicted in the right panels is needed). We note that it is not obvious *a priori* how the modes at  $\sim 32$  and  $\sim 55\text{ cm}^{-1}$  ( $\gamma_{a1}$ ) are related to the mode at  $\sim 44\text{ cm}^{-1}$  ( $\gamma_a$ ). However, the relative intensity behavior of these two modes suggests that they might not be ground state heme coherences (as discussed further below). The relative phases of the low-frequency vibrational modes can be obtained with an approximate error of  $\pm\pi/8$  using the LPSVD analysis, and these are listed for the strong low frequency modes in the Supporting Information (Table S3). No dramatic phase shift of these modes was observed except for the phase flip of  $\gamma_a$  between 412, 416, and 443 nm.

## DISCUSSION

In this study, we measured the low frequency vibrational coherence spectra of ferric cyt *c* as a function of excitation

wavelength in the region 412–443 nm on the red side of the Soret band. Because low frequency modes below  $200\text{ cm}^{-1}$  are thermally excited at room temperature ( $k_B T \sim 300\text{ K} \sim 200\text{ cm}^{-1}$ ), they are potential candidates to be involved as reaction coordinates that are critical to protein function. For example, the heme doming mode, found in the  $35\text{--}50\text{ cm}^{-1}$  region for 5-coordinate ferrous heme, has been shown to play an important role as a reaction coordinate for the binding of CO.<sup>46,47</sup> On the other hand, for heme mediated electron transport, it is thought that distortions and thermal excitation of the heme ruffling mode can affect both the redox properties and the kinetics for heme reduction.<sup>10,34,35,48,49</sup> It has also been shown that when large ruffling distortions are present, as in cytochrome *c*, the intensity of modes with ruffling content will be enhanced.<sup>28</sup> Thus, the study of the low frequency heme vibrations of cyt *c*, using VCS at different excitation wavelengths, helps to reveal the behavior of modes with large ruffling content as well as offering the possibility to detect the presence of underlying resonant charge-transfer excited states. The mode frequencies of the charge transfer state may differ from the ground state ferric heme because of perturbations that reflect the transient electronic rearrangement.

As shown in Figure 5, the vibrational coherence spectra at 412 and 416 nm show a strong mode near  $44\text{ cm}^{-1}$  ( $\gamma_a$ ), which is thought to have significant ruffling content.<sup>21</sup> For excitation between 421 and 435 nm, there is a gradual appearance of a new mode near  $\sim 55\text{ cm}^{-1}$  ( $\gamma_{a1}$ ) as well as another lower frequency mode in the range  $\sim 20\text{--}35\text{ cm}^{-1}$ . The unusual change in the relative amplitudes of these modes relative to  $\gamma_a$  as a function of the pump–probe wavelength may be related to underlying charge transfer (CT) electronic excitations that have coherence frequencies that differ from the ground state. The general trend in the region between 425 and 432 nm can be explained by a dip in the intensity of  $\gamma_a$  and an increase in the intensity of  $\gamma_{a1}$  (see the Supporting Information, Figure S3). (Note that a mode near  $30\text{ cm}^{-1}$  is also observed to increase,

along with an even lower frequency feature at  $19\text{ cm}^{-1}$ . However, features below  $\sim 20\text{ cm}^{-1}$  must be viewed with caution because they approach the critical damping threshold where their time-dependent signals can become entangled with the monotonic population responses.) It appears that the  $\sim 30\text{ cm}^{-1}$  mode intensity peaks slightly to the blue of the  $55\text{ cm}^{-1}$  ( $\gamma_{a1}$ ) mode, but both of these modes are clearly appearing at excitations that are significantly to the red of the ferric ground state Soret band maximum located at  $409\text{ nm}$ . Still further to the red at  $443\text{ nm}$ , the  $\gamma_a$  mode reappears, but it is oppositely phased with respect to excitation in the  $412\text{--}416\text{ nm}$  range. The very different trend in the relative intensities of  $\gamma_a$  and  $\gamma_{a1}$  suggests that they may be associated with different electronic excitations.

We therefore tentatively assign the  $\gamma_{a1}$  mode to ruffling in an excited charge transfer (CT) state where the iron atom has  $d^6$  electronic character and the ruffling mode is expected to have a higher frequency. The NSD analysis in the Supporting Information (Figures S5.1 and S5.2) indicates a smaller ruffling distortion is present in the reduced form of many cyt *c* systems.<sup>50–52</sup> Moreover, a quantitative analysis of the mode frequencies as a function of ruffling distortion, using an anharmonic Morse potential, indicates that mode softening occurs as more ruffling distortion is applied<sup>34,53</sup> (see below). Thus, we expect that a  $d^6$  iron atom associated with a transient CT state will have less ruffling and a higher frequency, which is consistent with the assignment of  $\gamma_{a1}$  to ruffling in the putative CT state.

The observed frequency shift of  $\sim 10\text{ cm}^{-1}$  ( $44\text{--}55\text{ cm}^{-1}$ ) is quantitatively predicted using the anharmonic model discussed in section S6 of the Supporting Information. From Figure S5.2 (Supporting Information), we deduce that there is a roughly  $\sim 35\%$  reduction in the ruffling distortion upon going from a  $d^5$  to a  $d^6$  iron in the various species where structures are available (Figures S5.1 and S5.2, Supporting Information). Translated to hh cyt *c*, this suggests that the ruffling equilibrium position shifts from  $q_0 \sim 3.5\text{ amu}^{1/2}\text{ \AA}$ , as seen in the X-ray structure for the ferric  $d^5$  configuration, to  $q_0 \sim 2.3\text{ amu}^{1/2}\text{ \AA}$  (or less, if the NMR structure in Figure S5.1, Supporting Information, is correct) when the iron is in the  $d^6$  configuration. Using the linear correlation between the ruffling frequency and the heme ruffling distortion presented in Figure S6.1 (Supporting Information), we see that, when  $\gamma_a$  is found at  $44\text{ cm}^{-1}$  in the  $d^5$  ferric state, the ruffling frequency for the  $d^6$  state is predicted to be  $57\text{ cm}^{-1}$  (due to the shift of  $q_0$  from  $\sim 3.5$  to  $\sim 2.3\text{ amu}^{1/2}\text{ \AA}$ ).

The phase and intensity behavior of the  $\gamma_a$  mode is very similar to observations made in previous studies of the NO and  $\text{CN}^-$  adducts of myoglobin,<sup>32,54</sup> where unexpected dips of intensity accompanied by phase flips occur roughly  $20\text{ nm}$  to the red of the Soret band maximum. In the case of MbCN, where  $\text{CN}^-$  turns out to be the photolabile ligand,<sup>55</sup> the phase jump and intensity dip occurs at  $\sim 418\text{ nm}$ , which is  $23\text{ nm}$  to the red of the 5-coordinate histidine-ligated ferric photoproduct Soret band maximum at  $395\text{ nm}$ .<sup>56</sup>

The observation of phase flips and intensity dips removed by  $\sim 20\text{ nm}$  from the maximum of the resonant absorption band can be explained; however, in order to do so, we must go beyond the linearly coupled harmonic oscillator theory,<sup>41,42</sup> which predicts such behavior at the maximum of the resonant absorption band. One simple explanation involves an optical line shape that depends quadratically upon the underlying distribution of nuclear coordinate equilibrium positions. This is

a type of coupling that has been shown to underlie the asymmetric broadening of the Soret band in deoxy myoglobin.<sup>57,58</sup> Thus, if the coordinate distribution is excited into coherent motion, the Soret bandwidth, in addition to its centroid, will be modulated. This type of “quadratic” coupling results in a phase jump and intensity minimum that occurs on either side of the Soret maximum, and we suggest that strong quadratic effects underlie the “anomalous” phase and intensity behavior observed both here and in previous studies.<sup>32,54</sup>

In contrast to  $\gamma_a$ , the presence of strong relative amplitude for  $\gamma_{a1}$  in the  $425\text{--}435\text{ nm}$  region (see Figure 5 and Figure S3, Supporting Information) suggests that it may be coupled to an electronic excitation other than the Soret band. The reduction of the  $\gamma_a$  mode intensity in this region opens a window to reveal the underlying coherence activity related to this other excitation. As demonstrated in previous VCS studies, the intensity of the dichroic coherent signal does not maximize precisely at the maximum of the resonant electronic transition but rather a few nm away<sup>38,41,42</sup> on either the red or blue sides of the absorption maximum (found at  $409\text{ nm}$  for ferric cyt *c*). However, the presence of a relative intensity maximum in  $\gamma_{a1}$  at  $\sim 430\text{ nm}$  indicates that it is unlikely to be a ground state coherence that is coupled to the Soret band. As a result, we suggest that its activity is related to a CT excitation that could arise either from a direct radiative transition to an excited state that underlies the Soret band or from an ultrafast nonradiative decay process that involves a transient CT state.

As mentioned previously, the heme cofactor in cyt *c* has a highly ruffled geometry. The ruffling distortion tilts the  $p_z$  orbitals of the porphyrin nitrogens away from the heme normal and thereby increases the overlap of the porphyrin  $\pi$  and iron  $d_{xy}$  orbitals. At the same time, this distortion partially disrupts the Fe  $3d_{xz}$  and  $3d_{yz}$  ( $d\pi$ ) mixing with the porphyrin orbitals.<sup>10,59</sup> In addition, the Fe  $3d_\pi$  orbitals can also mix with His imidazole  $\pi$  orbitals and with the Met sulfur lone pair.<sup>10</sup> As a result, there is a rich set of possible direct CT excitations that involve the iron and the porphyrin.<sup>60</sup> However, given the much slower nonradiative decay that is observed when  $\text{Zn}^{2+}(d^{10})$  replaces the open shell iron atom,<sup>61</sup> it is very likely that, following photoexcitation of the porphyrin  $\pi^*$  orbital, the ultrafast nonradiative electronic decay<sup>62</sup> takes place via vacancies in the iron d orbital manifold. Such a nonradiative channel has been proposed to explain other studies in model compounds<sup>63</sup> and heme proteins.<sup>64,65</sup> In the context of the VCS measurements, this process can be considered analogous to a “reaction” where an electron moves from the porphyrin  $\pi^*$  orbital into an unfilled state of the ferric iron d orbitals. Low-frequency coherences coupled to this type of electronic excitation will be similar to those observed in other photochemical reactions and should be most easily revealed when the  $\gamma_a$  mode, associated with the “reactant” ferric cyt *c* ground state, minimizes its amplitude in the  $425\text{--}435\text{ nm}$  region. Just as for direct optical excitation of a CT state, transients involving population of the iron 3d orbitals can be formed during ultrafast<sup>18,62,66</sup> nonradiative decay on time scales that are less than the  $\sim 50\text{ fs}$  laser pulse width.

In order to check for the presence of direct underlying charge transfer states, we compared the Soret absorption at low ( $20\text{ K}$ ) and room ( $295\text{ K}$ ) temperature in a glycerol and water ( $70:30$ ) mixture, as shown in Figure S7 of the Supporting Information. The low temperature absorption spectrum of the ferrous form is consistent with earlier reports, which reveal an underlying transition near  $434\text{ nm}$  that was assigned to a CT band.<sup>67,68</sup>



This underlying transition on the red edge of the main absorption band is revealed because the broadening, associated with low frequency chromophore/protein vibrational modes,<sup>69</sup> is removed at low temperature.<sup>67,70</sup> On the other hand, a similar underlying transition is not observed in ferric cyt *c*, but this could be due to the additional broadening that arises from the shorter excited state lifetime in the ferric form.<sup>18,62,66</sup> Obviously, these measurements do not address the possibility of the ultrafast nonradiative population of a d<sup>6</sup> iron CT state, which is also expected to have an underlying transition near 434 nm.

We must also note that the relative absorption cross section (or “oscillator strength”) of an underlying charge transfer band will be smaller (by at least 10<sup>2</sup>) compared to the Soret band. However, a CT excitation is generally more localized compared to an extended  $\pi$ – $\pi^*$  transition. Thus, the electron–nuclear coupling strength, which measures the transient forces applied to the nuclei by the electronic state change, is expected to be larger for a CT transition. Moreover, coherent motion on an excited state surface will generally lead to significantly larger signals than a corresponding ground state coherence signal.<sup>41,42</sup> This can be traced to the fact that the ground state coherent wavepacket is limited to motion on the scale of its width on the initial ground state surface. In contrast, the excited state wavepacket can move a significant distance from the Franck–Condon region, generating large signals, especially for final electronic states that involve substantial electron rearrangement (such as bond breaking or electron transfer). Both of these effects (larger electron–nuclear coupling and larger excited state vs ground state coherence signals) will be operative regardless of the excitation channel (e.g., ultrafast nonradiative decay involving a CT state<sup>63–65</sup> or direct photon excitation of a CT band). As a result, the coherence signals from a CT state may be comparable to those from a ground-state coherence.

The above discussion suggests that the ruffling mode must be strongly coupled if it is to be observed following excitation of a CT state. We can estimate the electron–nuclear coupling for the CT state, if we note that the mass-weighted equilibrium position of the ruffling mode in cyt *c* shifts from  $q_0 \sim 3.5 \text{ amu}^{1/2} \text{ \AA}$  to  $q_0 \sim 2.5 \text{ amu}^{1/2} \text{ \AA}$  when the heme iron atom is changed from a d<sup>5</sup> to a d<sup>6</sup> configuration (see the Supporting Information, Figure S5.2). If we make a reasonable estimate for the reduced mass of the ruffling mode ( $\sim 100 \text{ amu}$ ), we find that a shift on the order of 0.1 Å should follow excitation of an electron into the vacant iron d orbital. As a point of reference, the typical shifts for the extended  $\pi$ – $\pi^*$  orbital excitations in heme are on the order of 0.01 Å.<sup>67,69,71</sup> Because the electron–nuclear coupling scales with the square of the equilibrium shift following electronic excitation, it suggests that the electron–nuclear coupling of the CT excitation should be roughly 100 times larger than what is found for a  $\pi$ – $\pi^*$  excitation. Moreover, as discussed above and in the Supporting Information (section S6), the equilibrium shift of the putative CT state leads to a ruffling frequency increase from 44 to 57 cm<sup>−1</sup>, which is very close to what is observed. More generally, the strong coupling of the ruffling mode to the iron-centered CT excitation makes it a likely candidate to be a thermally accessible reaction coordinate with the ability to modulate the propensity for heme electron transfer reactions.<sup>34,63,64</sup>

## SUMMARY

In summary, we have used femtosecond vibrational coherence spectroscopy to investigate the low frequency vibrational

modes of ferric cyt *c*. A mode near 55 cm<sup>−1</sup> ( $\gamma_{a1}$ ) was observed for excitations to the red of the Soret band, and it gains intensity as the excitation wavelength is tuned from 425 to 435 nm. Another strong mode ( $\gamma_a$ ) that we assign as a ground state ruffling coherence minimizes its intensity in this region, helping to facilitate the observation of  $\gamma_{a1}$  (which is also present at 412 and 443 nm but not clearly observable due to the strong 44 cm<sup>−1</sup> mode). The assignment of the modes  $\gamma_a$  and  $\gamma_{a1}$  to ground and excited (CT) state ruffling, respectively, is consistent with the anharmonic coupling model presented in the Supporting Information, as well as with other ruffling frequency assignments that are correlated with the magnitude of the heme ruffling distortion. The up-shifted frequency of the ruffling mode in the excited (CT) state, compared to the ground state, indicates that ferrous hh cytc has a smaller ruffling distortion than its ferric counterpart, which is consistent with its NMR structure and with X-ray structures of other cyt *c* species. This work, along with the structural studies, provides evidence that heme ruffling motion is strongly coupled to excitations that involve electron transfer into the vacant d <sub>$\pi$</sub>  orbital associated with the ferric iron atom.

## ■ ASSOCIATED CONTENT

### Supporting Information

The experimental details, the procedure for NSD analysis, resonance Raman spectra of ferric cyt *c* in the low and high frequency regions (Figure S1), the 18 ps optical response of ferric cyt *c* at 425 nm (Figure S2), the wavelength dependent amplitude of low-frequency vibrational modes (Figures S3 and S4), the NSD analysis of the oxidized and reduced heme in various cyt *c* species (Figures S5.1 and S5.2), anharmonic model correlating ruffling distortion and frequency (section S6), absorption spectra of ferric and ferrous forms of cyt *c* at low temperature (Figure S7), the time constants and amplitudes for the optical response of ferric cyt *c* (Table S1), the factors used to normalize the VCS data for different excitation wavelengths (Table S2), and the low frequency modes and their phases at different excitation wavelengths (Table S3. This material is available free of charge via the Internet at <http://pubs.acs.org>.

## ■ AUTHOR INFORMATION

### Corresponding Author

\*Phone: 617-373-5705. E-mail: [champ@neu.edu](mailto:champ@neu.edu).

### Present Address

<sup>‡</sup>Photosciences and Photonics Section, Chemical Sciences and Technology Division, National Institute for Interdisciplinary Science and Technology, CSIR, Trivandrum 695 019, Kerala, India.

### Author Contributions

<sup>†</sup>V.K. and Y.S. contributed equally to this work.

### Notes

The authors declare no competing financial interest.

## ■ ACKNOWLEDGMENTS

V.K. thanks the DST-SERC fast track scheme. This work is supported by a grant from the NSF (CHE-1243948) and partially by the NIH (DK35090). The authors thank Dr. Minoru Kubo, Dr. Flaviu Guria, and Mr. Alex Demidov for useful discussions.

## ■ REFERENCES

- (1) Ow, Y.-L. P.; Green, D. R.; Hao, Z.; Mak, T. W. Cytochrome c: Functions Beyond Respiration. *Nat. Rev. Mol. Cell Biol.* **2008**, *9*, 532–542.
- (2) Scott, R. A. *Cytochrome c: A Multidisciplinary Approach*; University Science Books: Sausalito, CA, 1996.
- (3) Cartling, B. In *Cytochrome c: In Biological Application of Raman Spectroscopy*; Spiro, T. G., Ed.; John Wiley: New York, 1988; Vol. 3, pp 217–248.
- (4) Negrerie, M.; Cianetti, S.; Vos, M. H.; Martin, J. L.; Kruglik, S. G. Ultrafast Heme Dynamics in Ferrous versus Ferric Cytochrome c Studied by Time-resolved Resonance Raman and Transient Absorption Spectroscopy. *J. Phys. Chem. B* **2006**, *110*, 12766–12781.
- (5) Zang, C.; Stevens, J. A.; Link, J. J.; Guo, L.; Wang, L.; Zhong, D. Ultrafast Proteinquake Dynamics in Cytochrome c. *J. Am. Chem. Soc.* **2009**, *131*, 2846–2852.
- (6) Wang, W.; Ye, X.; Demidov, A. A.; Rosca, F.; Sjödin, T.; Cao, W. X.; Sheeran, M.; Champion, P. M. Femtosecond Multicolor Pump-Probe Spectroscopy of Ferrous Cytochrome c. *J. Phys. Chem. B* **2000**, *104*, 10789–10801.
- (7) Lowenich, D.; Kleinermanns, K.; Karunakaran, V.; Kovalenko, S. A. Transient and Stationary Spectroscopy of Cytochrome c: Ultrafast Internal Conversion Controls Photoreduction. *Photochem. Photobiol.* **2008**, *84*, 193–201.
- (8) Bram, O.; Consani, C.; Cannizzo, A.; Chergui, M. Femtosecond UV Studies of the Electronic Relaxation Processes in Cytochrome c. *J. Phys. Chem. B* **2011**, *115* (46), 13723–13730.
- (9) Consani, C.; Bräm, O.; van Mourik, F.; Cannizzo, A.; Chergui, M. Energy transfer and relaxation mechanisms in Cytochrome c. *Chem. Phys.* **2012**, *396* (0), 108–115.
- (10) Liptak, M. D.; Wen, X.; Bren, K. L. NMR and DFT Investigation of Heme Ruffling: Functional Implications for Cytochrome c. *J. Am. Chem. Soc.* **2010**, *132*, 9753–9763.
- (11) Walker, F. A. Magnetic Spectroscopic (EPR, ESEEM, Mossbauer, MCD and NMR) Studies of Low-spin Ferriheme Centers and Their Corresponding Heme Proteins. *Coord. Chem. Rev.* **1999**, *186*, 471–534.
- (12) McDermott, P.; May, L.; Orlando, J. A. Mössbauer Study of Ferri- and Ferrocycytochrome c. *Biophys. J.* **1967**, *7* (5), 615–620.
- (13) Hu, S.; Morris, I. K.; Singh, J. P.; Smith, K. M.; Spiro, T. G. Complete Assignment of Cytochrome c Resonance Raman Spectra via Enzymic Reconstitution with Isotopically Labeled Hemes. *J. Am. Chem. Soc.* **1993**, *115*, 12446–12458.
- (14) Cianetti, S.; Negrerie, M.; Vos, M. H.; Martin, J. L.; Kruglik, S. G. Photodissociation of Heme Distal Methionine in Ferrous Cytochrome c Revealed by Subpicosecond Time-resolved Resonance Raman Spectroscopy. *J. Am. Chem. Soc.* **2004**, *126*, 13932–13933.
- (15) Leu, B. M.; Zhang, Y.; Bu, L. T.; Straub, J. E.; Zhao, J. Y.; Sturhahn, W.; Alp, E. E.; Sage, J. T. Resilience of the Iron Environment in Heme Proteins 6. *Biophys. J.* **2008**, *95* (12), 5874–5889.
- (16) Leu, B. M.; Ching, T. H.; Zhao, J. Y.; Sturhahn, W.; Alp, E. E.; Sage, J. T. Vibrational Dynamics of Iron in Cytochrome c 5. *J. Phys. Chem. B* **2009**, *113* (7), 2193–2200.
- (17) Leu, B. M.; Alatas, A.; Sinn, H.; Alp, E. E.; Said, A. H.; Yavas, H.; Zhao, J. Y.; Sage, J. T.; Sturhahn, W. Protein Elasticity Probed with Two Synchrotron-based Techniques. *J. Chem. Phys.* **2010**, *132*, 08S103-7.
- (18) Suemoto, T.; Ebihara, H.; Nakao, H.; Nakajima, M. Observation of Ultrafast Q-band Fluorescence in Horse Heart Cytochrome c in Reduced and Oxidized Forms. *J. Chem. Phys.* **2011**, *134*, 034502-5.
- (19) Jentzen, W.; Song, X. Z.; Shelhutt, J. A. Structural Characterization of Synthetic and Protein-bound Porphyrins in Terms of the Lowest-frequency Normal Coordinates of the Macrocyclic. *J. Phys. Chem. B* **1997**, *101*, 1684–1699.
- (20) Ma, J.-G.; Vanderkooi, J. M.; Zhang, J.; Jia, S.-L.; Shelhutt, J. A. Resonance Raman Investigation of Nickel Microperoxidase-11. *Biochemistry* **1999**, *38*, 2787–2795.
- (21) Sun, Y.; Karunakaran, V.; Champion, P. M. Investigations of the Low-Frequency Spectral Density of Cytochrome c upon Equilibrium Unfolding. *J. Phys. Chem. B* **2013**, *117*, 9615–9625.
- (22) Jentzen, W.; Ma, J. G.; Shelhutt, J. A. Conservation of the Conformation of the Porphyrin Macrocyclic in Hemoproteins. *Biophys. J.* **1998**, *74*, 753–763.
- (23) Shokhireva, T. K.; Berry, R. E.; Uno, E.; Balfour, C. A.; Zhang, H. J.; Walker, F. A. Electrochemical and NMR Spectroscopic Studies of Distal Pocket Mutants of Nitrophorin 2: Stability, Structure, and Dynamics of Axial Ligand Complexes. *Proc. Natl. Acad. Sci. U.S.A.* **2003**, *100*, 3778–3783.
- (24) Zoppellaro, G.; Harbitz, E.; Kaur, R.; Ensign, A. A.; Bren, K. L.; Andersson, K. K. Modulation of the Ligand-Field Anisotropy in a Series of Ferric Low-Spin Cytochrome c Mutants derived from *Pseudomonas aeruginosa* Cytochrome c-551 and *Nitrosomonas europaea* Cytochrome c-552: A Nuclear Magnetic Resonance and Electron Paramagnetic Resonance Study. *J. Am. Chem. Soc.* **2008**, *130*, 15348–15360.
- (25) Bowman, S. E. J.; Bren, K. L. The Chemistry and Biochemistry of Heme c: Functional Bases for Covalent Attachment. *Nat. Prod. Rep.* **2008**, *25*, 1118–1130.
- (26) Hobbs, J. D.; Shelhutt, J. A. Conserved Nonplanar Heme Distortions in Cytochromes-C. *J. Protein Chem.* **1995**, *14*, 19–25.
- (27) Hagarman, A.; Wallace, C. J.; Laberge, M. M.; Schweitzer-Stenner, R. Out-of-plane Deformations of the Heme Group in Different Ferrocycytochrome c Proteins Probed by Resonance Raman Spectroscopy. *J. Raman Spectrosc.* **2008**, *39*, 1848–1858.
- (28) Kubo, M.; Gruia, F.; Benabbas, A.; Barabanschikov, A.; Montfort, W. R.; Maes, E. M.; Champion, P. M. Low-frequency Mode Activity of Heme: Femtosecond Coherence Spectroscopy of Iron Porphine Halides and Nitrophorin 2. *J. Am. Chem. Soc.* **2008**, *130*, 9800–9811.
- (29) Ionascu, D.; Gruia, F.; Ye, X.; Yu, A. C.; Rosca, F.; Beck, C.; Demidov, A.; Olson, J. S.; Champion, P. M. Temperature-Dependent Studies of NO Recombination to Heme and Heme Proteins. *J. Am. Chem. Soc.* **2005**, *127*, 16921–16934.
- (30) Pauleta, S. R.; Lu, Y.; Goodhew, C. F.; Moura, I.; Pettigrew, G. W.; Shelhutt, J. A. Calcium-dependent Heme Structure in the Reduced Forms of the Bacterial Cytochrome c Peroxidase from *Paracoccus pantotrophus*. *Biochemistry* **2008**, *47*, 5841–5850.
- (31) Karunakaran, V.; Denisov, I.; Sligar, S. G.; Champion, P. M. Investigation of the Low Frequency Dynamics of Heme Proteins: Native and Mutant Cytochrome P450cam and Redox Partner Complexes. *J. Phys. Chem. B* **2011**, *115*, 5665–5677.
- (32) Gruia, F.; Kubo, M.; Ye, X.; Champion, P. M. Investigations of Vibrational Coherence in the Low-frequency Region of Ferric Heme Proteins. *Biophys. J.* **2008**, *94*, 2252–2268.
- (33) Gruia, F.; Kubo, M.; Ye, X.; Ionascu, D.; Lu, C.; Poole, R. K.; Yeh, S. R.; Champion, P. M. Coherence Spectroscopy Investigations of the Low-frequency Vibrations of Heme: Effects of Protein-specific Perturbations. *J. Am. Chem. Soc.* **2008**, *130*, 5231–5244.
- (34) Sun, Y.; Benabbas, A.; Zeng, W.; Kleingardner, J. G.; Bren, K. L.; Champion, P. M. Investigations of Heme Distortion, Low-Frequency Vibrational Excitations, and Electron Transfer in Cytochrome c. *Proc. Natl. Acad. Sci. U.S.A.* **2014**, *111*, 6570–6575.
- (35) Walker, F. A. Models of the Bis-Histidine-Ligated Electron-Transferring Cytochromes. Comparative Geometric and Electronic Structure of Low-Spin Ferro- and Ferrihemes. *Chem. Rev.* **2004**, *104*, 589–616.
- (36) Olea, C.; Kuriyan, J.; Marletta, M. A. Modulating Heme Redox Potential through Protein-Induced Porphyrin Distortion. *J. Am. Chem. Soc.* **2010**, *132* (37), 12794–12795.
- (37) Zhu, L.; Li, P.; Huang, M.; Sage, J. T.; Champion, P. M. Real time observation of low frequency heme protein vibrations using femtosecond coherence spectroscopy. *Phys. Rev. Lett.* **1994**, *72* (2), 301–304.
- (38) Rosca, F.; Kumar, A. T. N.; Ye, X.; Sjödin, T.; Demidov, A. A.; Champion, P. M. Investigations of Coherent Vibrational Oscillations in Myoglobin. *J. Phys. Chem. A* **2000**, *104*, 4280–4290.



- (39) Karunakaran, V.; Benabbas, A.; Youn, H.; Champion, P. M. Vibrational Coherence Spectroscopy of the Heme Domain in the CO-Sensing Transcriptional Activator CooA. *J. Am. Chem. Soc.* **2011**, *133* (46), 18816–18827.
- (40) Ruhman, S.; Joly, A. G.; Nelson, K. A. Time-resolved Observations of Coherent Molecular Vibrational Motion and the General Occurrence of Impulsive Stimulated Scattering. *J. Chem. Phys.* **1987**, *86*, 6563–6565.
- (41) Kumar, A. T. N.; Rosca, F.; Widom, A.; Champion, P. M. Investigations of Amplitude and Phase Excitation Profiles in Femtosecond Coherence Spectroscopy. *J. Chem. Phys.* **2001**, *114*, 701–724.
- (42) Kumar, A. T. N.; Rosca, F.; Widom, A.; Champion, P. M. Investigations of Ultrafast Nuclear Response Induced by Resonant and Nonresonant Laser Pulses. *J. Chem. Phys.* **2001**, *114*, 6795–6815.
- (43) Karunakaran, V.; Benabbas, A.; Sun, Y. H.; Zhang, Z. Y.; Singh, S.; Banerjee, R.; Champion, P. M. Investigations of Low-Frequency Vibrational Dynamics and Ligand Binding Kinetics of Cystathionine beta-Synthase. *J. Phys. Chem. B* **2010**, *114*, 3294–3306.
- (44) Gruia, F.; Ye, X.; Ionascu, D.; Kubo, M.; Champion, P. M. Low Frequency Spectral Density of Ferrous Heme: Perturbations Induced by Axial Ligation and Protein Insertion. *Biophys. J.* **2007**, *93*, 4404–4413.
- (45) Constantine, S.; Zhou, Y.; Morais, J.; Ziegler, L. D. Dispersed Optical Heterodyne Detected Birefringence and Dichroism of Transparent Liquids. *J. Phys. Chem. A* **1997**, *101*, 5456–5462.
- (46) Ye, X.; Ionascu, D.; Gruia, F.; Yu, A.; Benabbas, A.; Champion, P. M. Temperature-dependent Heme Kinetics with Nonexponential Binding and Barrier Relaxation in the Absence of Protein Conformational Substates. *Proc. Natl. Acad. Sci. U.S.A.* **2007**, *104*, 14682–14687.
- (47) Benabbas, A.; Karunakaran, V.; Youn, H.; Poulos, T. L.; Champion, P. M. Effect of DNA Binding on Geminate CO Recombination Kinetics in CO-sensing Transcription Factor CooA. *J. Biol. Chem.* **2012**, *287*, 21729–21740.
- (48) Shelnutt, J. A.; Song, X. Z.; Ma, J. G.; Jia, S. L.; Jentzen, W.; Medforth, C. J. Nonplanar Porphyrins and Their Significance in Proteins. *Chem. Soc. Rev.* **1998**, *27*, 31–41.
- (49) Paulat, F.; Lehnert, N. Detailed Assignment of the Magnetic Circular Dichroism and UV–vis Spectra of Five-Coordinate High-Spin Ferric [Fe(TPP)(Cl)]. *Inorg. Chem.* **2008**, *47*, 4963–4976.
- (50) Banci, L.; Bertini, I.; Huber, J. G.; Spyroulias, G. A.; Turano, P. Solution Structure of Reduced Horse Heart Cytochrome c. *J. Biol. Inorg. Chem.* **1999**, *4*, 21–31.
- (51) Takano, T.; Dickerson, R. E. Redox Conformation Changes in Refined Tuna Cytochrome c. *Proc. Natl. Acad. Sci. U.S.A.* **1980**, *77*, 6371–6375.
- (52) Louie, G. V.; Brayer, G. D. High-resolution Refinement of Yeast Iso-1-cytochrome c and Comparisons with other Eukaryotic Cytochromes c. *J. Mol. Biol.* **1990**, *214*, 527–555.
- (53) Sun, Y. Investigations of Protein Induced Heme Distortion Using Raman and Vibrational Coherence Spectroscopy. Northeastern University, Boston, MA, 2013.
- (54) Rosca, F.; Kumar, A. T. N.; Ionascu, D.; Ye, X.; Demidov, A. A.; Sjodin, T.; Wharton, D.; Barrick, D.; Sligar, S. G.; Yonetani, T.; Champion, P. M. Investigations of Anharmonic Low-Frequency Oscillations in Heme Proteins<sup>†</sup>. *J. Phys. Chem. A* **2001**, *106*, 3540–3552.
- (55) Zeng, W.; Sun, Y.; Benabbas, A.; Champion, P. M. Investigations of Ferric Heme Cyanide Photodissociation in Myoglobin and Horseradish Peroxidase. *J. Phys. Chem. B* **2013**, *117*, 4042–4049.
- (56) Cao, W.; Christian, J. F.; Champion, P. M.; Rosca, F.; Sage, J. T. Water Penetration and Binding to Ferric Myoglobin. *Biochemistry* **2001**, *40*, 5728–5737.
- (57) Srajer, V.; Schomacker, K. T.; Champion, P. M. Spectral Broadening in Biomolecules. *Phys. Rev. Lett.* **1986**, *57*, 1267–1270.
- (58) Srajer, V.; Reinisch, L.; Champion, P. M. Investigation of Laser-Induced Long-Lived States of Photolyzed MbCO. *Biochemistry* **1991**, *30*, 4886–4895.
- (59) Schejter, A.; Eaton, W. A. Charge-transfer Optical Spectra, Electron Paramagnetic Resonance, and Redox Potentials of Cytochromes. *Biochemistry* **1984**, *23*, 1081–1084.
- (60) Eaton, W. A.; Hofrichter, J. Polarized Absorption and Linear Dichroism Spectroscopy of Hemoglobin. *Methods Enzymol.* **1981**, *76*, 175–261.
- (61) Adar, F.; Gouterman, M.; Aronowitz, S. Fluorescence, resonance Raman, and radiationless decay in several hemoproteins. *J. Phys. Chem.* **1976**, *80* (20), 2184–2191.
- (62) Champion, P. M.; Lange, R. On the Quantitation of Light Emission from Cytochrome c in the Low Quantum Yield Limit. *J. Chem. Phys.* **1980**, *73*, 5947–5957.
- (63) Rury, A. S.; Sension, R. J. Broadband Ultrafast Transient Absorption of Iron (III) Tetraphenylporphyrin Chloride in the Condensed Phase. *Chem. Phys.* **2013**, *422*, 220–228.
- (64) Lim, M.; Jackson, T. A.; Anfinrud, P. A. Femtosecond Near-IR Absorbance Study of Photoexcited Myoglobin: Dynamics of Electronic and Thermal Relaxation. *J. Phys. Chem.* **1996**, *100*, 12043–12051.
- (65) Ishizaka, S.; Wada, T.; Kitamura, N. Femtosecond Transient Absorption Study on Relaxation Intermediates in Oxy-myoglobin. *Photochem. Photobiol. Sci.* **2009**, *8*, 562–566.
- (66) Bräm, O.; Consani, C.; Cannizzo, A.; Chergui, M. Femtosecond UV Studies of the Electronic Relaxation Processes in Cytochrome c. *J. Phys. Chem. B* **2011**, *115*, 13723–13730.
- (67) Schomacker, K. T.; Champion, P. M. Investigations of Spectral Broadening Mechanisms in Biomolecules: Cytochrome c. *J. Chem. Phys.* **1986**, *84*, 5314–5325.
- (68) Champion, P. M.; Collins, D. W.; Fitchen, D. B. Resonance Raman Spectra of Heme Proteins at Low Temperature. *J. Am. Chem. Soc.* **1976**, *98* (22), 7114–7115.
- (69) Champion, P. M.; Albrecht, A. C. On Band Shapes of Electronic Transitions in the Multimode Weak Coupling Limit. *J. Chem. Phys.* **1980**, *72*, 6498–6506.
- (70) Champion, P. M.; Albrecht, A. C. Resonance Raman Scattering: The Multimode Problem and Transform Methods. *Annu. Rev. Phys. Chem.* **1982**, *33*, 353–376.
- (71) Schomacker, K. T.; Bangcharoenpaupong, O.; Champion, P. M. Investigations of the Stokes and Anti-Stokes Resonance Raman Scattering of Cytochrome c. *J. Chem. Phys.* **1984**, *80*, 4701–4717.